JOURNAL OF GEOPHYSICAL RESEARCH, VOL. 117, E00L12, doi:10.1029/2012JE004159, 2012

Low-degree structure in Mercury's planetary magnetic field

Brian J. Anderson,[1] Catherine L. Johnson,[2,3] Haje Korth,[1] Reka M. Winslow,[2] Joseph E. Borovsky,[4] Michael E. Purucker,[5] James A. Slavin,[6] Sean C. Solomon,[7,8] Maria T. Zuber,[9] and Ralph L. McNutt Jr.[1]

Received 8 June 2012; revised 19 October 2012; accepted 22 October 2012; published 7 December 2012.

[1] The structure of Mercury's internal magnetic field has been determined from analysis of orbital Magnetometer measurements by the MESSENGER spacecraft. We identified the magnetic equator on 531 low-altitude and 120 high-altitude equator crossings from the zero in the radial cylindrical magnetic field component, B_ρ. The low-altitude crossings are offset 479 ± 6 km northward, indicating an offset of the planetary dipole. The tilt of the magnetic pole relative to the planetary spin axis is less than 0.8°. The high-altitude crossings yield a northward offset of the magnetic equator of 486 ± 74 km. A field with only nonzero dipole and octupole coefficients also matches the low-altitude observations but cannot yield off-equatorial $B_\rho = 0$ at radial distances greater than 3520 km. We compared offset dipole and other descriptions of the field with vector field observations below 600 km for 13 longitudinally distributed, magnetically quiet orbits. An offset dipole with southward directed moment of 190 nT-R_M^3 yields root-mean-square (RMS) residuals below 14 nT, whereas a field with only dipole and octupole terms tuned to match the polar field and the low-altitude magnetic equator crossings yields RMS residuals up to 68 nT. Attributing the residuals from the offset-dipole field to axial degree 3 and 4 contributions we estimate that the Gauss coefficient magnitudes for the additional terms are less than 4% and 7%, respectively, relative to the dipole. The axial alignment and prominent quadrupole are consistent with a non-convecting layer above a deep dynamo in Mercury's fluid outer core.

Citation: Anderson, B. J., C. L. Johnson, H. Korth, R. M. Winslow, J. E. Borovsky, M. E. Purucker, J. A. Slavin, S. C. Solomon, M. T. Zuber, and R. L. McNutt Jr. (2012), Low-degree structure in Mercury's planetary magnetic field, *J. Geophys. Res.*, *117*, E00L12, doi:10.1029/2012JE004159.

1. Introduction

[2] The discovery of Mercury's internally generated magnetic field by the Mariner 10 spacecraft [*Ness et al.*, 1974, 1975] presented an enigma: the large-scale structure of the field suggested a dynamo origin, but the observed field strength was one or more orders of magnitude less than that predicted by scaling arguments and the fields measured at other planets [*Stevenson*, 2003]. Alternative explanations included long-wavelength crustal remanence [e.g., *Aharonson et al.*, 2004] and thermoelectric currents at the core–mantle boundary [e.g., *Stevenson*, 1987; *Giampieri and Balogh*, 2002].

[3] The recent finding that at least a layer of the core remains molten at present [*Margot et al.*, 2007] favors a dynamo source rather than remanent magnetization for the origin of the field [*Aharonson et al.*, 2004]. This interpretation is further supported by magnetic field observations taken during the first two flybys of Mercury by the MErcury Surface, Space ENvironment, GEochemistry, and Ranging (MESSENGER) spacecraft, which revealed a dominantly dipolar field, with no evidence for large-scale remanent crustal fields [*Anderson et al.*, 2008; *Purucker et al.*, 2009; *Uno et al.*, 2009]. A variety of core structures and dynamo regimes have been demonstrated to yield planetary dipole moments that are sufficiently weak to be compatible with observations of Mercury's magnetic field. These include thin-shell dynamos [e.g., *Stanley et al.*, 2005; *Takahashi and Matsushima*, 2006], deep dynamos [*Heimpel et al.*, 2005], deep dynamos enclosed by a stably stratified, electrically conductive layer [*Christensen*, 2006; *Wicht et al.*, 2007; *Christensen and Wicht*, 2008; *Manglik et al.*, 2010], induction feedback on the convecting

[1]Space Department, The Johns Hopkins University Applied Physics Laboratory, Laurel, Maryland, USA.
[2]Department of Earth and Ocean Sciences, University of British Columbia, Vancouver, British Columbia, Canada.
[3]Planetary Science Institute, Tucson, Arizona, USA.
[4]Space Science Institute, Boulder, Colorado, USA.
[5]NASA Goddard Space Flight Center, Greenbelt, Maryland, USA.
[6]Department of Atmospheric, Oceanic and Space Sciences, University of Michigan, Ann Arbor, Michigan, USA.
[7]Department of Terrestrial Magnetism, Carnegie Institution of Washington, Washington, D. C., USA.
[8]Lamont-Doherty Earth Observatory, Columbia University, Palisades, New York, USA.
[9]Department of Earth, Atmospheric and Planetary Sciences, Massachusetts Institute of Technology, Cambridge, Massachusetts, USA.

Corresponding author: B. J. Anderson, Space Department, The Johns Hopkins University Applied Physics Laboratory, 11100 Johns Hopkins Rd., MS B200-E230, Laurel, MD 20723-6099, USA. (brian.anderson@jhuapl.edu)

0148-0227/12/2012JE004159

portions of the core from magnetopause currents [*Glassmeier et al.*, 2007a, 2007b; *Gómez-Pérez and Solomon*, 2010; *Gómez-Pérez and Wicht*, 2010; *Heyner et al.*, 2011a, 2011b], and precipitation of solid iron in radial zones within a liquid outer core [*Vilim et al.*, 2010].

[4] Recent orbital observations from MESSENGER confirm that the planetary field can be represented as a nearly axially aligned dipole. However, not only is the dipole moment weak, but it is also offset by 0.19 R_M (where R_M is Mercury's mean radius, 2440 km) to the north. This offset is equivalent to axial dipole, g_{10}, and quadrupole, g_{20}, terms in a spherical harmonic representation in the ratio $g_{20}/g_{10} = 0.4$ [*Anderson et al.*, 2011]. Such a result is consistent with prior modeling from flyby observations [*Uno et al.*, 2009; *Alexeev et al.*, 2010] and helps clarify why the MESSENGER equatorial flybys, inbound from the tail dusk side, all passed through the southern magnetotail lobe [*Anderson et al.*, 2010].

[5] The combination of a large quadrupole term with close alignment of the weak field to the planetary rotation axis presents a challenge to existing dynamo models. Downward continuation of an axial field with the inferred g_{20}/g_{10} ratio yields a field at the core-mantle boundary that is still dipole-dominated but with a large quadrupole term. Conventional dynamos, in which the top of the convecting layer coincides with the top of the core, have difficulty in producing such a field. Multipolar dynamos can produce a weak field [e.g., *Olson and Christensen*, 2006], but such fields are not dipole dominated. Thin-shell dynamos can produce weak fields but show a dipole offset much less than observed at Mercury [*Stanley et al.*, 2005], or equivalently no clear dominance of harmonic degree 2 (i.e., quadrupole) over higher degrees in the power spectra [*Heimpel et al.*, 2005; *Takahashi and Matsushima*, 2006]. The feedback-dynamo process yields a planetary field that is axisymmetric and dominated by odd harmonics [*Heyner et al.*, 2011b], and the influence of iron snow layers also produces a field with a large octupole (degree 3) contribution and comparatively weak quadrupole structure [*Vilim et al.*, 2010]. In another class of models, sub-adiabatic heat flow at the core-mantle boundary produces a stably stratified layer. This stable, electrically conductive layer filters out the spherical harmonic terms of high degree and order that are strong in the field at the top of the dynamo region, but that also vary the most in time. In these models the field at the planetary surface is dominated by the axial dipole and quadrupole terms that are the most slowly time-varying components [*Stevenson*, 1982; *Christensen*, 2006; *Wicht et al.*, 2007; *Christensen and Wicht*, 2008]. In addition, zonal flows set up in the stably stratified layer preferentially reduce non-axisymmetric, low-degree terms [*Christensen and Wicht*, 2008], yielding a surface field that is weak, is dipole dominated, has a substantial quadrupole component, and is axisymmetric. Although these models are promising, the stable layer thickness, its dynamics (e.g., the role of double diffusion), and the resulting heat transport have been shown to affect markedly the observable field structure [*Stanley and Mohammadi*, 2008; *Manglik et al.*, 2010].

[6] The implications of the offset dipole result therefore warrant a critical examination of the initial findings from Mercury orbital data. The *Anderson et al.* [2011] analysis identified the magnetic equator from the spacecraft position at the point where the radial component of the magnetic field (B_ρ) vanished in a cylindrical coordinate system in which the cylinder axis, or z-axis, is aligned with the planetary spin axis, i.e., where the magnetic field was parallel to the spin axis. Interpretation of these observations is not unambiguous, however, because it is possible for more complex field geometries not indicative of an offset dipole to yield surfaces on which $B_\rho = 0$. For example, a field with a dipole and large octupole terms but a small quadrupole term, as predicted by the induction feedback mechanism of *Heyner et al.* [2011a, 2011b], will yield three surfaces on which $B_\rho = 0$, and it is possible that only the most northern of these might be detectable with a spacecraft in an orbit as eccentric as that of MESSENGER.

[7] In this paper we examine the MESSENGER magnetic field data from Mercury orbit in detail to assess the uniqueness of the $B_\rho = 0$ signature as an indicator of the magnetic equator. We also present initial analyses of higher-degree structure in the axial field to more firmly distinguish among candidate models for the planetary field generation.

[8] In Section 2, we present an in-depth analysis of the magnetic equator signatures, including distant crossings of the magnetotail current sheet. The possibility that the observed signatures reflect centered, axially aligned, odd harmonic fields is assessed quantitatively. In Section 3, the analysis is expanded to a comparison of the observed vector fields over all longitudes against the most likely candidates for the planetary field to quantify the degree of correspondence between the global vector magnetic field and different hypothetical global fields. The results are summarized and discussed in Section 4.

2. Magnetic Equator Analysis

[9] Here we present a more extended analysis of the $B_\rho = 0$ signature than in our earlier report [*Anderson et al.*, 2011] by considering both the descending-node, lower-altitude equator crossings as well as the more distant ascending-node equator crossings. The magnetic equator determination is particularly valuable for analysis of MESSENGER orbital observations. Using only multivariable, nonlinear inversions to solve for Mercury's internal field is problematic for several reasons [cf. *Johnson et al.*, 2012]. First, high plasma pressures and corresponding magnetization currents are prevalent below 0.5 R_M altitude and within ~45° latitude of the equator and cause depressions in the magnetic field strength from tens of percent to over 90% [*Anderson et al.*, 2010; *Korth et al.*, 2011, 2012; *Winslow et al.*, 2012]. Second, external fields make contributions comparable to the internal field even at the planetary surface, so their effects must be quantitatively included [e.g., *Alexeev et al.*, 2008, 2010]. Because plasma pressure locations and densities vary from orbit to orbit [e.g., *Korth et al.*, 2012], however, the errors in the external field corrections for individual orbits can be large. Moreover, one cannot solve for the external field using the potential formalism because the sampled region is not free of currents. Finally, the MESSENGER orbit is eccentric and there is a northern hemispheric bias in low-altitude sampling, leading to high covariance among terms of low degree and order in the inversions [*Korth et al.*, 2004]. Restricting data to latitudes poleward of 45°N exacerbates the covariance problem.

[10] We therefore opted to determine the magnetic equator first and use this as a constraint on the inversions. For Mercury, the flyby observations showed that the dipole field

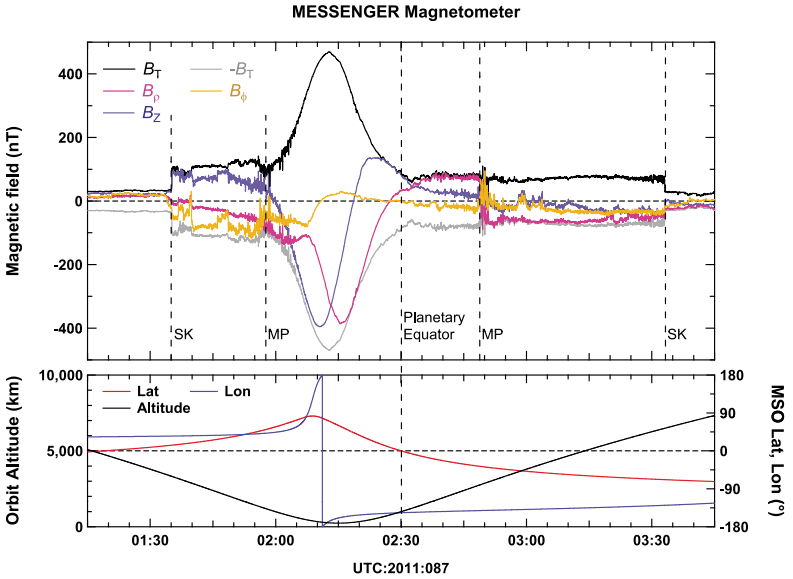

Figure 1. MESSENGER magnetic field and trajectory data for the Mercury magnetospheric transit on 28 March 2011, day of year (DOY) 087, from 01:30 to 03:30 UTC. (top) The 1-s averaged magnetic field data in MSO cylindrical coordinates (B_ρ, B_ϕ, B_Z) together with the field magnitude, B_T, and its negative, $-B_T$. (bottom) Spacecraft position in MSO coordinates: latitude, longitude, and altitude above the planetary surface. Longitude is measured positive eastward relative to the planet–Sun line such that $-90°$ is dawn, 0° is noon, 90° is dusk, and 180° ($-180°$) is midnight. The bow shock and magnetopause boundaries are indicated by vertical dashed lines labeled SK and MP, respectively. The descending-node planetary equator crossing, 0° geographic latitude, is also indicated.

is close to axially aligned [*Ness et al.*, 1975; *Anderson et al.*, 2008], and this geometry yields a particularly well-defined magnetic equator. If the planetary moment is axially aligned and perpendicular to the solar wind flow direction, the external currents (magnetopause and cross-tail currents) are centered on the magnetic equator and do not influence its location. Thus, for Mercury, the magnetic equator can be determined without making any corrections for the external fields and is an accurate independent constraint for both the external field description and inversion analyses [cf. *Johnson et al.*, 2012].

[11] For our analysis, we use Mercury solar orbital (MSO) coordinates, for which the Cartesian (X, Y, Z) components are as follows: Z is positive along the planetary spin axis, X is positive toward the Sun, and Y completes the right-hand system, positive duskward. Data are also analyzed in MSO cylindrical coordinates (ρ, ϕ, Z), where the unit vectors, $\mathbf{n}$, are defined as follows: $\mathbf{n}_\phi$ is positive eastward in the plane parallel to the planetary equator, $\mathbf{n}_Z$ is northward, and $\mathbf{n}_\rho$ completes the right-hand system such that $\mathbf{n}_\rho = \mathbf{n}_\phi \times \mathbf{n}_Z$.

[12] The MESSENGER spacecraft [*Solomon et al.*, 2007] entered orbit about Mercury on 18 March 2011. The initial spacecraft orbit had a periapsis altitude of 200 km, 82.5° inclination, 15,300 km apoapsis altitude, and 12-h period [cf. *Zurbuchen et al.*, 2011]. Data in this study are from the MESSENGER Magnetometer [*Anderson et al.*, 2007] from 23 March 2011, shortly after orbit insertion, through 2 March 2012. For this date range the ascending and descending orbit segments crossed the planetary equator at altitudes from 1000 to 1500 km, and from 3500 to 5000 km, respectively.

2.1. Descending-Node Equator Crossings

[13] Magnetic field and trajectory data are shown in Figure 1 for the first magnetospheric transit on 28 March 2011. The bow shock and magnetopause crossings identified from the rotations in the magnetic field are indicated along with the planetary equator crossing. The spacecraft was inbound in the afternoon near 45° MSO longitude, crossed the descending orbit node in the early morning near $-135°$ MSO longitude, and exited the magnetosphere 18 min later. The maximum field magnitude occurred slightly before the minimum altitude, consistent with the contributions from the magnetopause and tail current systems.

[14] On the descending orbit segment near 02:30 UTC the B_ρ component reversed sign from negative to positive several minutes prior to and north of the planetary equator crossing. When $B_\rho = 0$ nT near 02:27:30 UTC, the field was nearly purely northward with $B_\phi \sim 0$ nT. An expanded-time view of the equator crossing in Figure 2 shows the same magnetic field and spacecraft latitude data but instead of planetocentric distance gives the angle between $\mathbf{n}_\rho$ and the magnetic field defined as $\cos^{-1}(B_\rho/B_T)$, where B_T is the total magnetic field magnitude. This angle changed from near 160°, reflecting an inward-directed field, passed through 90° at the magnetic equator, and then decreased below 30° as the spacecraft passed into the southern magnetotail lobe. The magnetic equator crossing preceded the planetary equator by ~150 s, and at the planetary equator B_ρ was ~30 nT.

[15] To quantify the spacecraft position when B_ρ passes through zero, we consider Z_{MSO} as a function of B_ρ as shown in Figure 3 for four sequential descending-node equator

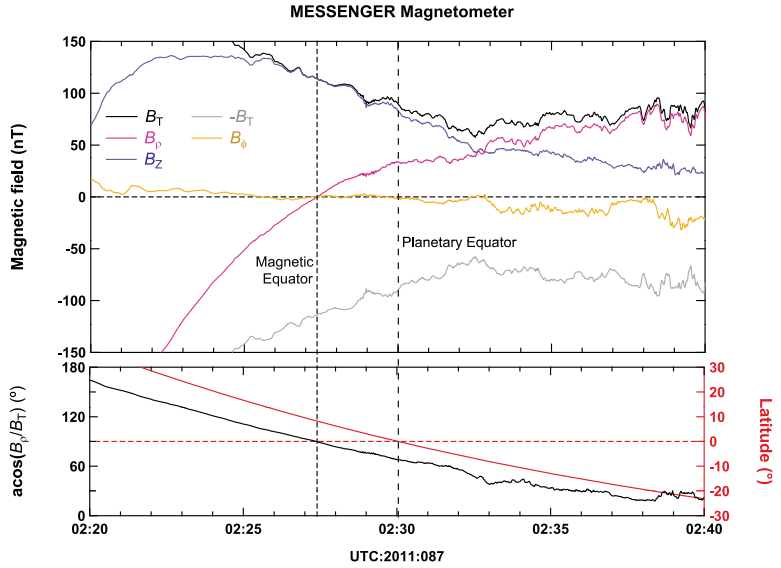

Figure 2. Expanded plot of MESSENGER Magnetometer data from Figure 1, 28 March 2011, focusing on the planetary equator crossing near 02:30 UTC. (top) The 1-s averaged magnetic field in MSO cylindrical coordinates in the same format as the top panel in Figure 1. (bottom) Angle between the magnetic field and $\mathbf{n}_\rho$, $\cos^{-1}(B_\rho/B_T)$, and spacecraft MSO latitude. The vertical dashed lines indicate times when the spacecraft passed through the magnetic equator (close-spaced dashes) and the planetary equatorial plane (wide-spaced dashes). The $B_\rho = 0$ point occurs at a planetary latitude of ∼10° and ∼150 s prior to the equator crossing.

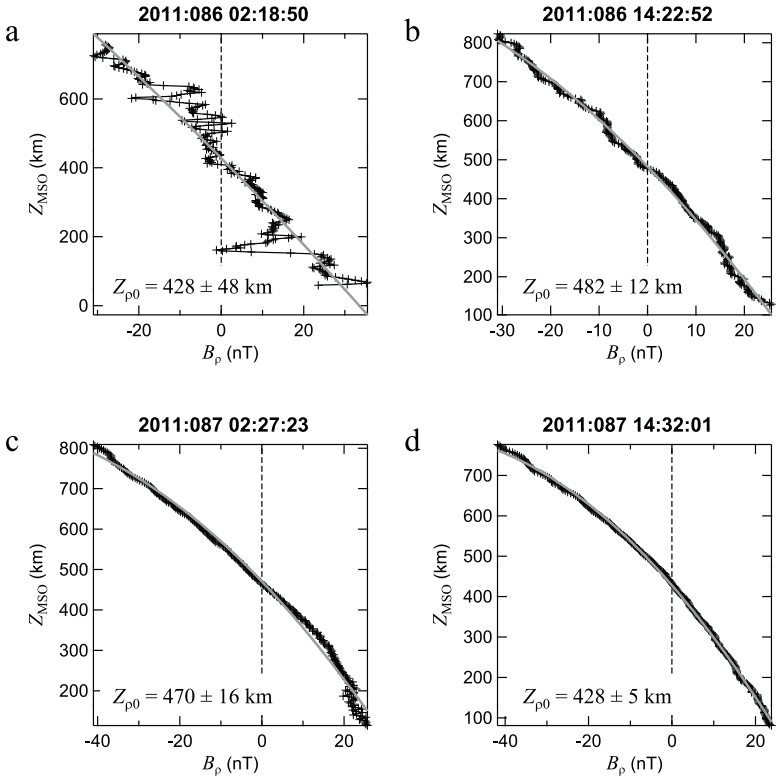

Figure 3. Spacecraft Z_{MSO} position plotted versus B_ρ for four segments of data near the descending-node equator crossings for four consecutive orbits from 27 and 28 March 2011 (DOY 86 and 87). Observations are plotted as plus symbols connected by solid thin black lines, and quadratic fits are shown by the thick gray lines. The $Z_{\rho 0}$ values for each pass obtained by the fits are indicated in each panel; uncertainties in the fit intercepts are three-standard-error estimates.

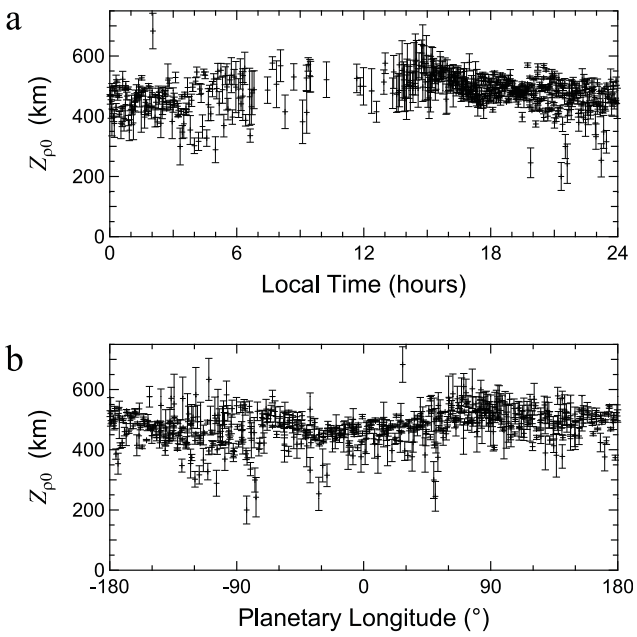

Figure 4. Magnetic equator crossing points, $Z_{\rho 0}$, versus (a) MSO local time and (b) planetary longitude derived from all MESSENGER Magnetometer data from Mercury orbit between 24 March 2011 and 2 March 2012. Vertical error bars show three-standard-error estimates in $Z_{\rho 0}$. The lack of values in the morning hours results from the fact that MESSENGER encounters the magnetopause before crossing the magnetic equator. Note that the average apparent local time of the solar wind ram direction is near 11 h MSO, so that the times of sparse data are nearly centered on the solar wind ram direction. The systematic variation in $Z_{\rho 0}$ with either local time or longitude has an amplitude of ~50 km (100 km peak to peak), about 10% of the offset.

crossings on 27 and 28 March 2011. The example from Figures 1 and 2 is in Figure 3c. These cases also show quadratic fits to Z_{MSO}. The $B_\rho = 0$ intercept of each fit gives an estimate of Z at the magnetic equator crossing for that pass, denoted as $Z_{\rho 0}$. The standard error estimate of the intercept is used as a measure of confidence in the $Z_{\rho 0}$. Note that near the $B_\rho = 0$ point we do not observe $dB_\rho/dZ \sim 0$. This is an important feature to be compared with the forward modeling of dipole-octupole models considered in Section 4.

[16] Corresponding fits were performed to all of the descending-node equator crossing data from 24 March 2011 to 2 March 2012. The results for the 531 near-planet equator crossings identified are shown in Figure 4. When the descending node was on the dayside, the spacecraft often encountered the magnetopause either before or nearly coincident with the $B_\rho = 0$ point, so $Z_{\rho 0}$ values were not obtained in these cases. The $Z_{\rho 0}$ data suggest a possible ~50 km amplitude variation such that $Z_{\rho 0}$ is greater at noon than at midnight. The average radial spacecraft distance corresponding to these crossings was ~3400 km, so the variation in $Z_{\rho 0}$ corresponds to a peak-to-peak latitude variation of ~1.5°. The mean $Z_{\rho 0}$, the mean standard error, and the average of $Z_{\rho 0}$ weighted by the inverse of the standard errors are given in Table 1 together with the altitude range of the points. The mean and weighted mean $Z_{\rho 0}$ values are not significantly different, but we consider the weighted mean to be slightly more reliable and adopt the value 479 ± 6 km as the offset value from these data.

[17] With this value for the offset we next assess the tilt in the field relative to the planetary rotation axis. To quantify the tilt of the offset dipole we transform the position and magnetic field data into a body-fixed coordinate system offset 479 km to the north along the planetary rotation axis, which we term the Mercury MAGnetic (MMAG) coordinate system, and we evaluate the latitude for which the radial field component, $B_{\text{r-MMAG}}$, in this system vanishes. The latitudes of the $B_{\text{r-MMAG}} = 0$ points give the magnetic dip latitude of each crossing in the MMAG system. The results of this analysis are shown in Figure 5. To determine the plane that contains the dip equator, we fit these data with a sine function, and the amplitude of this fit yields a tilt of

Table 1. Average Magnetic Offset $Z_{\rho 0}$ Values, Uncertainties, and ρ Range and Mean Values for Descending (Near) and Ascending (Far) Equator Crossings Derived From MESSENGER Magnetometer Data From 24 March 2011 Through 2 March 2012[a]

	Descending (Near)	Ascending (Far)	Units
Number of cases	531	120	n/a
Mean $Z_{\rho 0} \pm 3\sigma$	477 ± 7	420 ± 86	km
Mean 3σ	24	87	km
Weighted mean $Z_{\rho 0} \pm 3\sigma$	479 ± 6	486 ± 74	km
Mean $\rho_{\mathrm{MSO}} \pm$ sdev	3410 ± 110	6110 ± 470	km
$\rho_{\min}$, $\rho_{\max}$	3150, 3720	5240, 7560	km

[a]The uncertainties in the mean $Z_{\rho 0}$ values are three standard errors of the mean (3σ). The mean 3σ values are the averages of the 3σ standard errors in the $Z_{\rho 0}$ fit value for each equator crossing. The weighted mean $Z_{\rho 0}$ is the average $Z_{\rho 0}$ weighted by the inverse of the fit value standard errors. For the ρ_{MSO} statistics, sdev is the population standard deviation, whereas $\rho_{\min}$ and $\rho_{\max}$ are the minimum and maximum ρ_{MSO} values in each population.

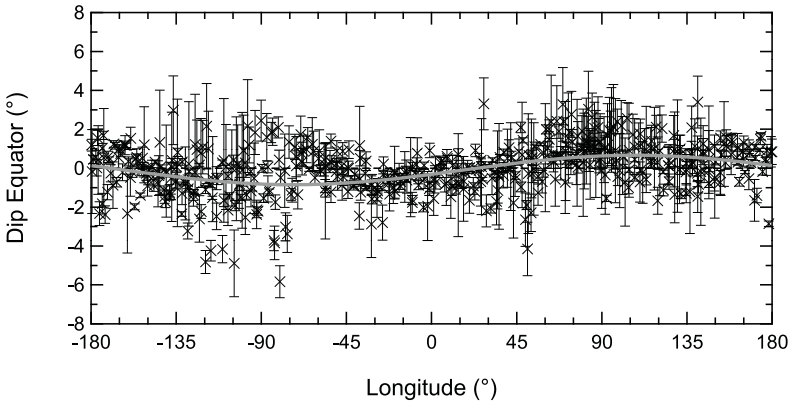

Figure 5. Dip equator latitude plotted versus planetary longitude. Data are shown by X symbols and error bars are three standard errors. The gray curve shows a sine fit constrained to have a period of 360° and corresponds to the best fit plane that represents the tilt of the magnetic equator relative to the planetary rotation axis. The resulting tilt is 0.8° with an azimuth (for the southern hemisphere pole) of −77° longitude. Because the data do not exhibit a strong 360° period, this tilt is considered an upper limit.

0.8°. Since the tilt signal is weak relative to the scatter in the data, we consider this result to be an upper limit, and we do not regard the longitude of the tilt as sufficiently constrained to report a value for it.

2.2. Ascending-Node Equator Crossings

[18] Here we present an analysis of the more distant crossings, which occurred from 3500 to 5000 km altitude in the magnetotail. If the near-planet equator crossings correspond to a true offset of the dipole, we expect that the more distant crossings would display a similar offset relative to the planetary equator. However, if the lower-altitude crossings were due to complex higher-degree structure in the field, these higher-degree terms should fall off more rapidly than the dipole and the higher-altitude magnetic equator would be shifted toward the planetary equator.

[19] An example ascending-node equator crossing on 24 November 2011 from 08:00 to 11:30 UTC is shown in Figure 6. The distant equator crossings occur in the magnetotail where the spacecraft transitions from the southern magnetotail lobe, within which the magnetic field is nominally anti-sunward and $\mathbf{B} \sim B_T \mathbf{n}_\rho$, to the northern magnetotail lobe where the field is nominally sunward and $\mathbf{B} \sim -B_T \mathbf{n}_\rho$. Coincident with the reversal in B_ρ is a depression in the total field indicative of the plasma pressure in the current sheet [*Korth et al.*, 2011, 2012]. In this particular instance the

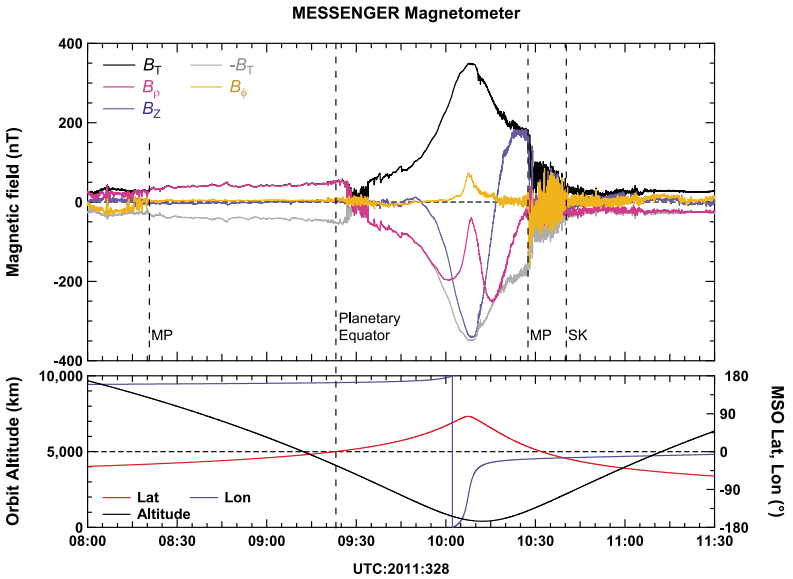

Figure 6. MESSENGER magnetic field data for the Mercury magnetospheric transit on 24 November 2011 (DOY 328) from 08:00 to 11:30 UTC in the same format as Figure 1, with the exception that the inbound bow shock crossing is omitted for clarity. The inbound bow shock crossing occurred at 05:45 UTC. The ascending-node planetary equator crossing, 0° latitude, is indicated near 09:23 UTC. The spacecraft was inbound in the late evening and crossed the ascending orbit node near midnight, at ∼170° MSO longitude. The outbound magnetopause was encountered prior to crossing the descending node equator.

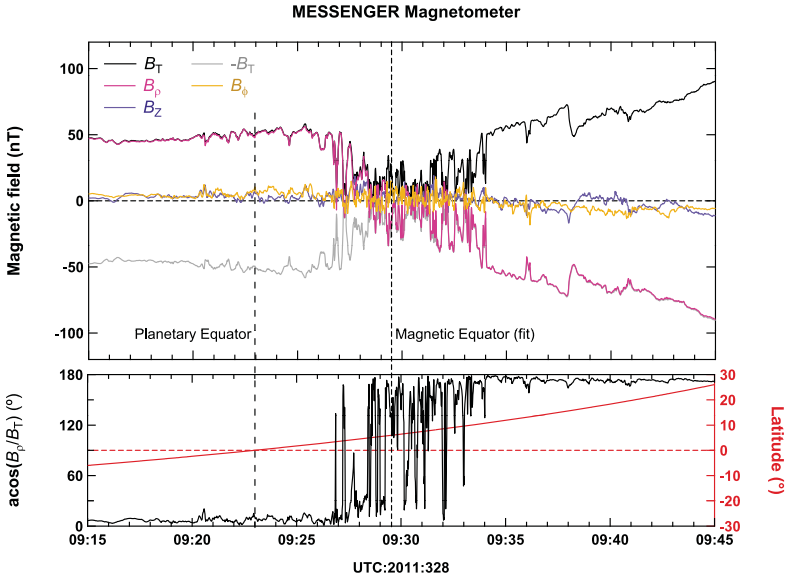

Figure 7. Expanded plot of MESSENGER Magnetometer data from Figure 6, 24 November 2011, focusing on the planetary equator crossing near 09:23 UTC in the same format as Figure 2.

current-sheet crossing started several minutes after the spacecraft crossed the magnetic equator, and the center of the current sheet was crossed ~5 min after the planetary equator. The maximum magnetic field occurred slightly after the minimum altitude, consistent with the dayside enhancement of the polar field due to magnetopause currents. For the example in Figure 6, the outbound magnetopause was encountered prior to the descending-node equator crossing. The outbound shock crossing occurred at 10:40 UTC, although variability, which we attribute to foreshock dynamics, was evident until 11:00 UTC.

[20] An expanded view of the ascending-node equator and current sheet crossings on this orbit is shown in Figure 7. The depressions in B_T coincide with rotations in the field from the southern tail lobe ($\mathbf{B} \sim B_\rho \mathbf{n}_\rho$) to the northern lobe ($\mathbf{B} \sim -B_\rho \mathbf{n}_\rho$) as the spacecraft passed through the magnetotail plasma sheet and cross-tail current sheet. The current sheet crossing occurred over a span of ~7 min starting slightly more than 3 min after the planetary equator crossing. The azimuthal component in the field remained small throughout the crossing. In contrast to the lower-altitude equator passes, the passes through the deeper tail current sheet often exhibited multiple reversals in B_ρ, which we attribute to dynamics in the tail related to north–south motion of the tail, magnetic reconnection dynamics, and turbulence in the current sheet.

[21] The higher-altitude crossings were analyzed in the same manner as the lower-altitude crossings to determine a best fit $Z_{\rho 0}$ for each crossing. Plots of Z_{MSO} versus B_ρ are shown in Figure 8 for four sequential distant equator crossings on 24 and 25 November 2011. The greater variability in B_ρ for the distant tail crossings is evident, reflecting repeated passage of the current sheet back and forth over the spacecraft. The fit intercepts yield best estimates for the average equator for each crossing. The standard errors of the intercepts are correspondingly higher for these distant tail crossings.

[22] To compare the descending (near) and ascending (far) equator crossings we plot $Z_{\rho 0}$ versus ρ_{MSO} for all of the crossings in Figure 9. Due to the evolution of the MESSENGER spacecraft orbit, successive deep tail (or "long-eclipse") seasons occurred for trajectories progressively closer to the planet. There are only six equator crossings determined during the first, most distant, deep tail season, because the Magnetometer was powered off for most of the first of these seasons. The deep tail seasons correspond to times of longest passage of the spacecraft through the planetary shadow, times during which management of spacecraft power was needed. For the first tail season, the Magnetometer instrument was powered off to safeguard the spacecraft while the behavior of the power system in Mercury orbit during long-eclipse seasons was characterized. Fortunately, the power margins allowed Magnetometer operation through successive long-eclipse seasons.

[23] The scatter in the more distant tail crossings is considerable and is larger than the three-standard-error uncertainties, so the variability must be real. Nonetheless, the crossings are not centered on the planetary equator. The statistics for the distant tail crossings are given in Table 1. The mean and weighted mean values for the near and far equator crossings are in agreement, indicating that the cross-tail current above 3000 km altitude is offset to the north. This result is consistent with expectations for an offset dipolar planetary field that organizes the global-scale external current systems including the tail magnetopause and cross-tail currents such that the mean current sheet position corresponds to the dipole magnetic equator [cf. *Alexeev et al.*, 2008, 2010].

[24] The scatter in $Z_{\rho 0}$ for the distant equator crossings is larger than that for the near tail crossings, and we briefly consider the source of this variation. We first examined the IMF $B_{X\text{-}MSO}$ component derived from MESSENGER observations before and after each magnetospheric transit. As *Winslow et al.* [2012] have shown, the sign of the IMF $B_{X\text{-}MSO}$ component was generally consistent on the inbound and outbound MESSENGER spacecraft orbits, so this component should reliably indicate the IMF sector imposed on Mercury's magnetosphere at the time of the equator crossings. We found no correlation between $Z_{\rho 0}$ and IMF $B_{X\text{-}MSO}$, indicating that this quantity is not governing the scatter in Figure 9.

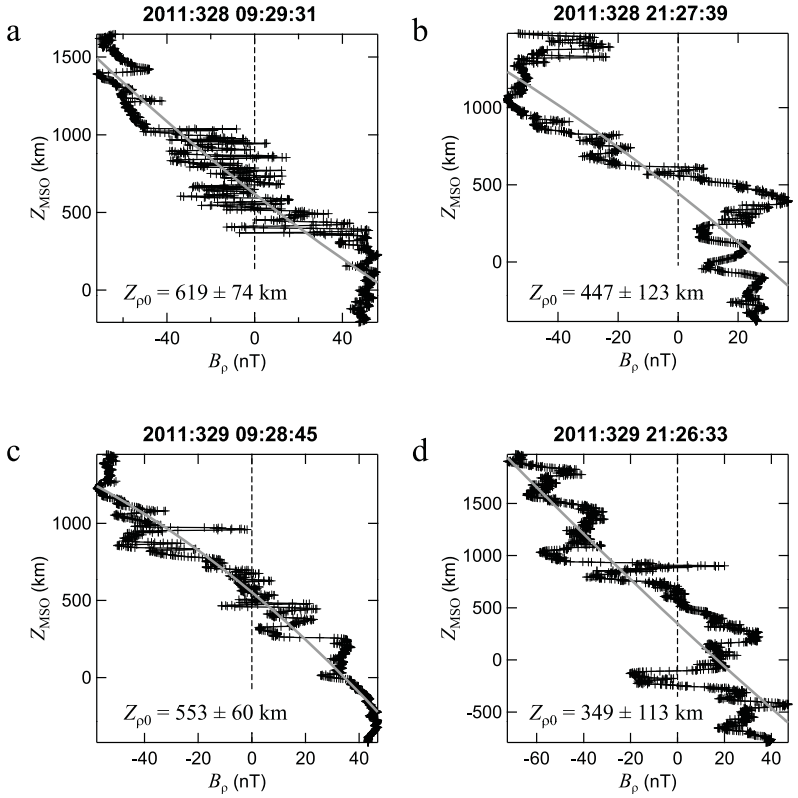

Figure 8. Spacecraft Z_{MSO} position plotted versus B_ρ for four segments of data near the ascending equator crossings from four consecutive Mercury orbits on 24 and 25 November 2011 (DOY 328 and 329) in the same format as Figure 3.

[25] We then divided the distant equator crossing events into three ranges of $Z_{\rho 0}$ with nearly equal numbers of events in each range, and we evaluated the average magnetic fields and positions as functions of time relative to the time of the current sheet crossing. The superposed epoch averages as functions of time relative to the fit $B_\rho = 0$ point are shown in Figure 10. The average $|B_\varphi|$ was very small, so we show only B_ρ and B_Z together with the total field, B_T. The angle relative to northward of the field projected onto the ρ-Z plane, $\theta_{\rho\text{-}Z} = \tan^{-1}(B_\rho/B_Z)$, is also shown together with the difference between $\theta_{\rho\text{-}Z}$ for the southernmost and northernmost events, $\delta\theta_{\rho\text{-}Z} = \theta_{\rho\text{-}Z\text{-}S} - \theta_{\rho\text{-}Z,N}$. The number of events, the average, minimum and maximum $Z_{\rho 0}$, and the mean $\theta_{\rho\text{-}Z}$ for the low, medium, and high $Z_{\rho 0}$ ranges used are given in Table 2.

[26] The Z component in the southern lobe, before the current sheet crossing, is consistently more positive for the northernmost than for the southernmost events. For the most southern $Z_{\rho 0}$ events, the magnetic field is tilted by 5° to 10° toward more positive $\theta_{\rho\text{-}Z}$ than for the most northern $Z_{\rho 0}$ events. The mean $\delta\theta_{\rho\text{-}Z}$ values for the southern lobe from 1500 to 1000 s and 1000 to 500 s before the current sheet crossing are 6.4° ± 0.2° and 5.3° ± 0.2°, and that for the northern lobe from 500 to 1000 s after the current sheet crossing is 6.06° ± 0.12°. These values are consistent with an overall southward tilt of the magnetotail for the southern $Z_{\rho 0}$ events relative to the northern $Z_{\rho 0}$ events and indicate that the spread in the $Z_{\rho 0}$ values is due to tilting of the tail northward or southward.

[27] To assess the source of the inferred north-south tail tilt, we consider the north–south excursions in solar wind velocity. Although MESSENGER does not measure the solar wind velocity, data from the Helios 1 and 2 spacecraft provide information regarding the excursions in solar wind

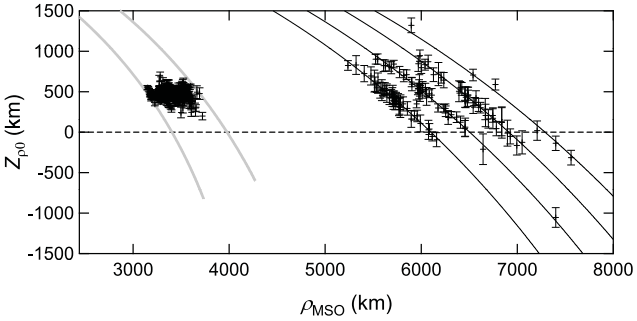

Figure 9. Magnetic equator crossing points, $Z_{\rho 0}$, plotted verses ρ_{MSO} for all crossings identified in data from 24 March 2011 through 2 March 2012. Vertical error bars indicate three standard errors for each $Z_{\rho 0}$ crossing point. Black curves show average trajectories for the four deep-tail seasons, and the thick light-gray curves show trajectory segments for the innermost and outermost orbits from which the lower-altitude equator crossings were identified.

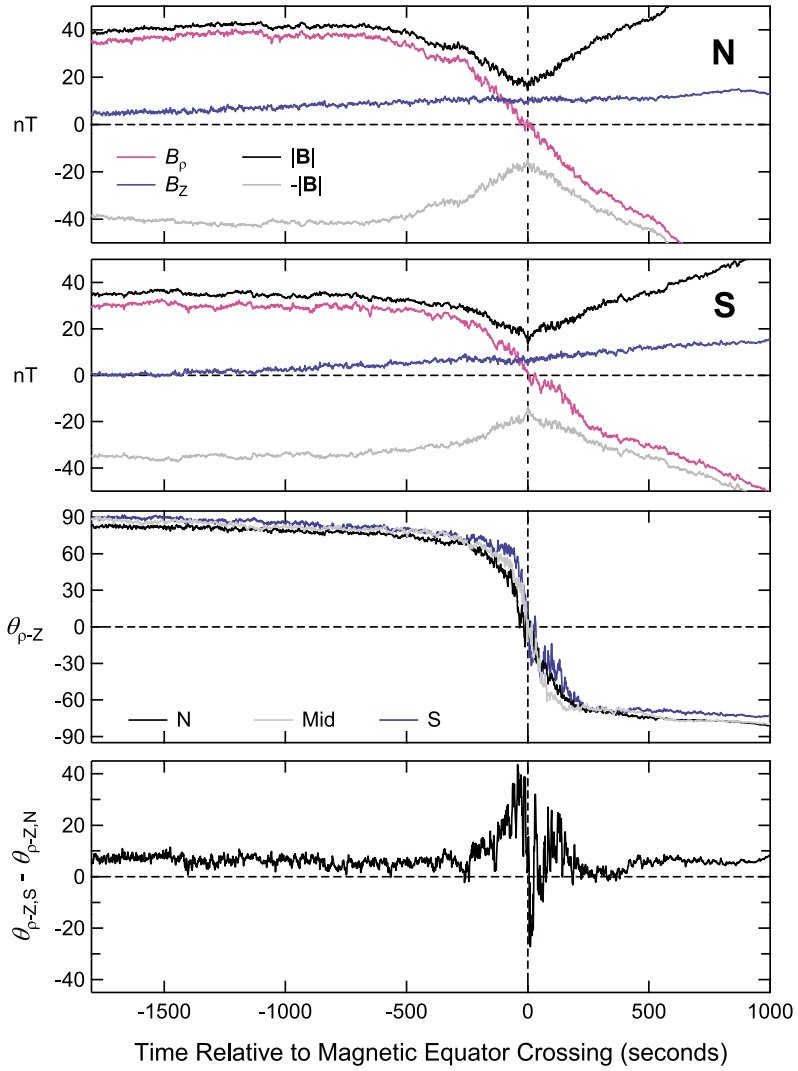

Figure 10. Superposed epoch analysis of magnetic field geometry for distant tail crossings. From top to bottom: total field |**B**|, B_ρ, B_Z, and $-|\mathbf{B}|$ for the northernmost (N) distant tail crossings; same quantities for the southernmost (S) distant tail crossings; $\theta_{\rho\text{-}Z}$, the tilt of the field in the ρ–Z plane from northward, with positive angles for positive ρ; the difference between $\theta_{\rho\text{-}Z}$ for southernmost and northernmost distant tail crossings.

velocity relative to the ecliptic plane at Mercury orbital distances. Plasma measurements [*Rosenbauer et al.*, 1977] in the slow solar wind from the Helios 1 and Helios 2 spacecraft were used to determine the angular deviation of the solar wind flow velocity from the radial direction [cf. *Borovsky*, 2012]. Using 40 s averages of the plasma flow velocity, the north-south deviation of flow was measured as $\theta_{\text{north-south}} = \sin^{-1}(V_{\text{SW-Z}}/V_{\text{SW}})$, where V_{SW} is the solar wind speed and $V_{\text{SW-Z}}$ is the component of the solar wind velocity perpendicular to the radial direction and out of the ecliptic, positive northward. In Figure 11, the distributions of $\theta_{\text{north-south}}$ are shown for two heliocentric distance ranges: 0.9–0.98 AU (blue curve) and 0.29–0.35 AU (red curve). The mean value and root-mean-square (RMS) deviation of the angular deviations are denoted in the figure. In the distance range 0.29–0.35 AU from the Sun, the measured deviations have an RMS spread of 3.9°, whereas near 1 AU the distribution is slightly less broad with an RMS of

Table 2. Statistics for Three $Z_{\rho 0}$ Ranges of Distant Tail Magnetic Equator Crossings[a]

$Z_{\rho 0}$ Range	Low	Medium	High	Units
Number of cases	40	42	40	n/a
$Z_{\rho 0}$ avg (min, max)	72 (−1054, 338)	493 (356, 604)	792 (614, 1320)	km
$\theta_{\rho\text{-}Z}$ southern lobe	82.3 ± 0.3	80.3 ± 0.2	77.0 ± 0.2	deg
$\theta_{\rho\text{-}Z}$ northern lobe	−71.2 ± 0.2	−77.1± 0.2	−77.3 ± 0.2	deg

[a]From top to bottom the rows give: the number of cases in each range; the average (avg), minimum (min), and maximum (max) $Z_{\rho 0}$; and the average $\theta_{\rho\text{-}Z} = \tan^{-1}(B_\rho/B_Z)$ for the southern and northern tail lobe intervals. The $\theta_{\rho\text{-}Z}$ averages were taken 500 to 1000 s before the magnetic equator crossing for the southern lobe and 500 to 1000 s after the magnetic equator crossing for the northern lobe. Uncertainties for $\theta_{\rho\text{-}Z}$ are three standard errors of the means.

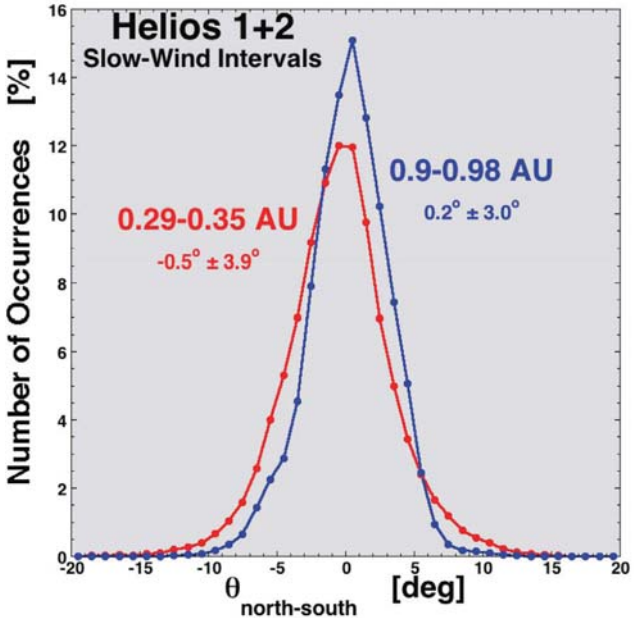

Figure 11. Angle of solar wind velocity relative to the ecliptic plane, $\theta_{\text{north-south}}$, derived from Helios 1 and 2 plasma observations, where positive angles are northward. Red curve shows the distribution for heliocentric distances from 0.29 to 0.35 AU, relevant to Mercury, and the blue curve shows the distribution from 0.9 to 0.98 AU heliocentric distance, comparable to Earth's orbit. The mean and root-mean-square $\theta_{\text{north-south}}$ values are indicated in the figure.

3.0°. The expected spread in north–south solar wind velocity is therefore consistent with the difference in magnetotail field observed for the southern and northern MESSENGER tail crossings. The magnetotail orientation will follow the solar wind flow direction, so we attribute the tail direction variability and the north–south variations in $Z_{\rho 0}$ for the distant tail crossings to north–south excursions of the solar wind velocity.

2.3. Quantitative Assessment of Dipole-Octupole Field Geometry

[28] To quantify the implication of the consistent Z_{MSO} offset of the magnetic equator signatures in the near and distant tail, we consider the structure of more complex axially aligned, centered magnetic fields. An axially aligned and centered dipole–octupole field, that is, with terms for degrees 1 and 3 in a spherical harmonic expansion, yields three surfaces on which $B_\rho = 0$, one of which is the planetary equator and the other two are symmetrically displaced to the north and south of the planetary equator. The ratio of the octupole to the dipole term falls off with distance r from the planet center of mass as $1/r^2$, so these surfaces should converge to the planetary equator with distance, and beyond some distance only the dipole $B_\rho = 0$ surface should remain. The ratio of average ρ_{MSO} values for the near and distant equator crossing populations is 1.8, so any octupole contribution is a factor of 3.2 less at the location of the ascending-node equator crossings than at the descending-node equator crossings. Also, north–south symmetric terms of odd higher spherical harmonic degree, 5 or greater, decrease at least as fast as $1/r^2$ relative to the octupole term, so the structure at MESSENGER orbit distances should be dominated by the dipole–octupole structure.

[29] We therefore consider a field with only g_{10} and g_{30} terms in the spherical harmonic expansion of the magnetic potential, ψ

$$\psi = R_M \sum_{l=0}^{\infty} \left(\frac{R_M}{r}\right)^{l+1} \sum_{m=0}^{l} (g_{lm}\cos(m\varphi) + h_{lm}\sin(m\varphi)) P_l^m(\cos\theta), \tag{1}$$

where (r, θ, φ) is the planetocentric position in spherical coordinates and the P_l^m are the Schmidt semi-normalized Legendre functions. Including only the g_{10} and g_{30} terms and writing the associated Legendre functions explicitly one finds

$$B_\rho = \frac{\sin 2\theta}{2r_M^3}\left\{3g_{10} + \frac{1}{2r_M^2}\left(35\cos^2\theta - 15\right)g_{30}\right\} \tag{2}$$

where $r_{\text{M}} = r/R_{\text{M}}$. Setting $G_{30} = g_{30}/g_{10}$ it immediately follows that the off-equator zeroes in B_ρ occur for

$$\cos\theta = \pm\sqrt{\frac{3}{7}\left(1 - \frac{2r_M^2}{5G_{30}}\right)} \tag{3}$$

and that multiple zeroes in B_ρ occur only for radial distances less than a critical distance r_{C}, i.e., where

$$r_{\text{M}} < r_{\text{C}}/r_{\text{M}} = \sqrt{\frac{5}{2}G_{30}}. \tag{4}$$

To yield $B_\rho = 0$ at the location of the lower-altitude equator crossing, ρ_{MSO} = 3409 km and Z_{MSO} = 477 km, requires $G_{30} = 0.546$ as obtained from (3). For this ratio, the maximum ρ at which an off-equatorial zero in B_ρ occurs is 3522 km, well below the minimum altitude of the distant equator crossings reported here.

[30] The curve for which $B_\rho = 0$ north of the planetary equator in a dipole–octupole field consistent with the average lower-altitude $B_\rho = 0$ point is shown in Figure 12 together

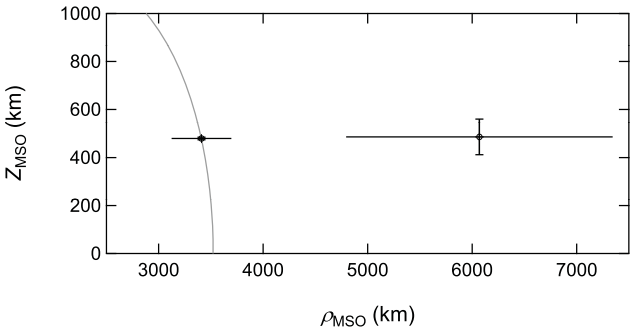

Figure 12. Plot of the average magnetic equator for the near-tail and deep-tail seasons (markers with error bars) together with Z_{MSO} points where a dipole–octupole field gives off-equatorial $B_\rho = 0$ (solid gray curve). Vertical error bars are 3 standard errors of the mean for each population of $Z_{\rho 0}$ values. Horizontal error bars show the ρ_{MSO} range of the observations. The dipole–octupole field was chosen to yield $B_\rho = 0$ at the mean location of the near-tail observations.

Table 3. Relationships Between Gauss Coefficients in Planet-Centered (Unprimed Quantities) and Axially Displaced (Primed Quantities) Coordinates in Terms of the Axial Offset, Δz_0, and Offset Magnetic Dipole $\mathbf{M} = (M, \theta_m, \phi_m)$

Degree	Planetocentric Coefficients	Offset Coefficients
1	$g_{10} = g'_{10}$	$g'_{10} = M\cos(\theta_m)$
	$g_{11} = g'_{11}$	$g'_{11} = M\sin(\theta_m)\cos(\phi_m)$
	$h_{11} = h'_{11}$	$h'_{11} = M\sin(\theta_m)\sin(\phi_m)$
2	$g_{20} = 2\Delta z_0 g'_{10}$	n/a
	$g_{21} = g'_{11}\Delta z_0/\sqrt{3}$	
	$h_{21} = h'_{11}\Delta z_0/\sqrt{3}$	
	$g_{22} = h_{22} = 0$	
3	$g_{30} = 3\Delta z_0^2 g'_{10}$	n/a
	$g_{31} = g'_{11}\Delta z_0^2/\sqrt{6}$	
	$h_{31} = h'_{11}\Delta z_0^2/\sqrt{6}$	
	$g_{3m} = h_{3m} = 0$ for $m > 1$	
4	$g_{40} = 4\Delta z_0^3 g'_{10}$	n/a

with the mean equator determinations from the low- and high-altitude populations of equator crossings. The horizontal lines for the near and distant magnetic equator crossings show the range of ρ_{MSO} for the observations. It is clear that the distant $B_\rho = 0$ observations cannot be explained under a dipole–octupole hypothesis, and the distant tail equator crossings are strong evidence for the offset in the planetary dipole field.

2.4. Offset Dipole and Gauss Coefficient Descriptions

[31] Representing the internal planetary field as an offset dipole is equivalent to a description in Mercury body fixed coordinates that is a series expansion in spherical harmonics with the contribution of each spherical harmonic term described by the Gauss coefficient. Table 3 gives the relationship between Gauss coefficients in the body-fixed frame and a dipole with moment M directed with a polar angle θ_m and azimuth ϕ_m, offset along the Z axis by Δz_0. The Gauss coefficients of the offset dipole in a coordinate system centered on the dipole, denoted by primes, are just the degree-1 terms, g'_{10}, g'_{11}, and h'_{11}. *Bartels* [1936] discussed the relationship between Gauss coefficients evaluated in two coordinate systems for which the axes are aligned but the origins are displaced. Here we consider only an axial displacement, Δz_0, along the z axis, expressed as a fraction of the mean planetary radius, and Table 3 gives the Gauss coefficients in the planet-centered system in terms of, Δz_0, g'_{10}, g'_{11}, and h'_{11}. The offset dipole yields Gauss coefficients of all degrees in the planet-centered system. The degree-one (dipole) coefficients in the offset and planet-centered systems are identical. Degree l terms are proportional to the product of the dipole term and Δz_0^l. Only the $m = 1$ non-axial terms are nonzero, because a tilted dipole has only order-one azimuthal structure.

[32] The results for the Mercury offset dipole obtained above are summarized in Table 4, which gives the offset dipole moment and orientation together with the corresponding values for the Gauss coefficients in the planet-centered system. Uncertainties are three-standard-error estimates. Since we derived only an upper limit on the dipole tilt of 0.8°, corresponding to $\theta_m > 179.2°$, we do not report a value for ϕ_m. The tilt upper limit corresponds to upper limits on the magnitude of the $m = 1$ off-axis terms. We report the off-axis upper limits only through $l = 3$ because they are already negligible for $l = 2$. Importantly, the large offset of the dipole along the rotation axis has substantial axial ($m = 0$) terms in the body-fixed spherical harmonic expansion up to and including the degree-4 coefficient, g_{40}. We emphasize that the values and limits in Table 4 are those implied by the offset dipole field. By superposition, contributions to coefficients of higher degree and order derived by subtracting from the observed planetary field the field of the offset dipole, may be summed with the values given here. We denote such residual contributions with an asterisk (*).

3. Forward-Model Comparison of Alternative Internal Fields

[33] The analysis above was based solely on the equator crossing points identified from $B_\rho = 0$. Here we consider data over as much of the orbit as possible to measure the agreement or disagreement between different models for the internal field. We use forward modeling to identify the dominant characteristics of the internal field. Because the external and

Table 4. Properties of Mercury's Internal Planetary Magnetic Field[a]

Quantity	Value
Δz_0	479 ± 6 km
$\Delta z_0/R_M$	0.196 ± 0.002
M	190 ± 10 nT-R_M^3
θ_m	>179.2°
ϕ_m	n/a[b]
g_{10}	−190 ± 10 nT
$\sqrt{(g_{11}^2 + h_{11}^2)}/g_{10}$	<0.014
$\sqrt{(g_{11}^2 + h_{11}^2)}$	<2.7 nT
g_{20}/g_{10}	0.392 ± 0.010
g_{20}	−74.6 ± 4.0 nT
$\sqrt{(g_{21}^2 + h_{21}^2)}/g_{10}$	<0.0016
$\sqrt{(g_{21}^2 + h_{21}^2)}$	<0.3 nT
g_{22}, h_{22}	0[c]
g_{30}/g_{10}	0.116 ± 0.009
g_{30}	−22.0 ± 1.3 nT
$\sqrt{(g_{31}^2 + h_{31}^2)}/g_{10}$	<0.0016
$\sqrt{(g_{31}^2 + h_{31}^2)}$	<0.3 nT
g_{3m}, h_{3m} for $m > 1$	0[c]
$\lvert g_{30}^*/g_{10}\rvert$	<0.04
g_{40}/g_{10}	0.030 ± 0.005
g_{40}	−5.7 ± 0.2 nT
$\lvert g_{40}^*/g_{10}\rvert$	<0.07

[a]Values for the dipole moment, axial offset, Δz_0, and magnetic dipole $\mathbf{M} = (M, \theta_m, \phi_m)$ as well as the corresponding Gauss coefficients are given in planet-centered coordinates. Uncertainties are 3σ standard errors. The quantities g_{30}^* and g_{40}^* are the contributions to the axial degree 3 and 4 coefficients in addition to those implied by the offset dipole.

[b]Reported coefficients are for zero tilt, $\theta_m = 180°$, for which the tilt longitude is not defined. The upper limit on the tilt of 0.8° was not judged sufficiently robust to warrant evaluation of ϕ_m.

[c]An axially offset dipole does not yield nonzero terms for orders greater than 1. Signals in residual fields from the axial offset dipole corresponding to non-axial coefficients of order higher than 1 are not estimated here, since the longitudinal structure in residuals appears to be ordered better in magnetospheric coordinates than in body-fixed coordinates.

Table 5. Representative Magnetic Equator Crossings With Low Standard Errors in $Z_{\rho 0}$ for Which the Magnetospheric Transits Were Used for Forward Model Comparisons[a]

Date (DOY)	$B_\rho = 0$ Time (hhmm)	$Z_{\rho 0}$ (km)	3σ $Z_{\rho 0}$ (km)	MSO LT (h)	Longitude (°E)
26 Mar 2011 (85)	1414	444.8	4.8	2.7	−142
1 Apr 2011 (91)	1507	491.4	5.4	0.7	−179
27 Apr 2011 (117)	1854	475.5	2.4	19.0	21
14 May 2011 (134)	2121	549.0	16.4	15.7	−85
20 Jun 2011 (171)	2349	442.1	4.8	3.2	47
4 Jul 2011 (185)	0630	434.0	2.5	23.2	−35
9 Jul 2011 (190)	0430	477.7	3.6	22.0	−65
17 Jul 2011 (198)	0120	456.3	3.3	20.4	−113
25 Sep 2011 (268)	1245	516.5	4.8	0.3	174
1 Oct 2011 (274)	0954	485.7	9.3	22.8	137
6 Oct 2011 (279)	0732	500.2	6.3	21.7	107
12 Oct 2011 (285)	0440	527.9	3.8	20.5	71
25 Oct 2011 (298)	1029	481.2	7.8	18.3	−10

[a]From left to right the columns give the date and day of year (DOY), the time for which the $Z_{\rho 0}$-B_ρ fit gives $B_\rho = 0$, the fit intercept for $Z_{\rho 0}$, the 3σ standard error in $Z_{\rho 0}$, the MSO local time (LT) in hours, and the longitude of the $B_\rho = 0$ point.

internal fields contribute approximately equally to the total magnetic field, even at the planetary surface, the challenge in applying standard spherical harmonic analyses to derive Mercury's internal field is substantial. *Johnson et al.* [2012] have discussed the derivation of an external model that is based on the parabolic magnetopause and magnetotail model of *Alexeev et al.* [2008, 2010] and for which the geometry and field intensity parameterizations are constrained by MESSENGER orbital observations. Here we present comparisons among candidate internal field models to which the external model derived by *Johnson et al.* [2012] has been added.

3.1. Forward Model Residuals for Magnetically Quiet Cases

[34] As *Slavin et al.* [2010] and numerous other authors have shown, magnetospheric dynamics at Mercury present strong variations in the observed magnetic field consistent with the presence of substantial scatter in the Z_{MSO} versus B_ρ data occasionally present (cf. Figures 3 and 8). We consider a subset of data selected to be as free of signatures of dynamics as possible, that is, for which the magnetic field data appear to vary smoothly throughout the magnetospheric transit and do not display prominent diamagnetic field depressions [e.g., *Korth et al.*, 2011, 2012] or substorm signatures [*Slavin et al.*, 2010, 2012; *Sundberg et al.*, 2012]. Moreover, we selected cases for which the standard error in the fit $Z_{\rho 0}$ was comparatively small. In addition, events were chosen to span all planetary longitudes. The set of events selected for this comparison is listed in Table 5.

[35] To illustrate the constraints that the orbital data place on the internal magnetic field, we evaluated the predictions of five different internal field models along the trajectories of each magnetospheric transit corresponding to the events in Table 5. To each of these models we added the external field model of *Alexeev et al.* [2010] with the parameters determined by *Johnson et al.* [2012] from MESSENGER orbital data. The five internal field models are (1) the offset, axially aligned dipole of *Johnson et al.* [2012] with a southward directed moment of 190 nT-R_M^3 and a northward offset of 0.196 R_M (i.e., that of Table 4); (2) an axially aligned, centered dipole with $g_{10} = -190$ nT; (3) an axially aligned, centered dipole with $g_{10} = -300$ nT, chosen to agree with the observed high-latitude field intensity; (4) an axially aligned, centered dipole–octupole field with $g_{10} = -190$ nT and $g_{30} = -158$ nT consistent with the g_{30} inferred from the observed near-planet $B_\rho = 0$ points; and (5) an axially aligned, centered dipole–octupole field with $g_{10} = -190$ nT and $g_{30} = -195$ nT to illustrate the effects of an even stronger octupole contribution.

[36] In Figure 13, we show a comparison of the B_ρ and B_Z observations for 26 March 2011 (DOY 85) from 14:00:37 UTC ($Z_{MSO} = 1.0\ R_M$) to 14:23:45 UTC ($Z_{MSO} = -0.5\ R_M$). It is clear that the offset dipole represents the data well (Figure 13 (top)). The centered dipole with $g_{10} = -190$ nT yields a field that is too weak at higher Z_{MSO}, and the centered dipole with $g_{10} = -300$ nT yields a B_ρ that is too broad and large at lower Z_{MSO}. The profiles of both centered dipole models are too broad, and only the offset dipole yields a field sufficiently focused at the higher Z_{MSO}. The B_Z component is also best fit by the offset dipole field.

[37] Since higher-degree terms in a spherical harmonic expansion can also focus regions of increased field strength poleward, we consider the simplest such field, a dipole–octupole field (Figure 13 (bottom)), for two possible octupole contributions. Both dipole–octupole models yield a field that is too concentrated at the pole. Moreover, they both yield a much weaker field within ~0.4 R_M of the equator than is observed. Both octupole models yield $B_\rho \sim 0$ over a broad range in Z_{MSO} near the equator and a B_Z that is too weak near the equator. For both dipole–octupole models, $dB_\rho/dZ \sim 0$ over a substantial region from $Z_{MSO} \sim 0$ to 0.3 R_M, which as noted above is not observed. Neither the B_ρ nor B_Z behavior near the equator is consistent with the observations. The descrepancies are large, often reaching ~100 nT.

[38] The same comparison between observations and the five internal field models is shown in Figure 14 for 25 October 2011 (DOY 298) from 10:14:24 UTC ($Z_{MSO} = 1.0\ R_M$) to 10:39:13 UTC ($Z_{MSO} = -0.5\ R_M$). This event shows essentially the same results: only the offset dipole yields an appropriately focused field at higher Z_{MSO} and a single clear magnetic equator. Only the residuals with the offset dipole are consistently low. All of the other models exhibit large systematic differences from the observations as functions of Z_{MSO}.

[39] The residuals at each Z_{MSO} were averaged over the orbits of Table 5, and the results are shown in Figure 15. Statistics given in Table 6 include the RMS residual, absolute residual, $|\delta|$, and standard deviation of the residuals, σ-δ, all averaged over Z_{MSO} as indicated by $\langle\rangle$. The centered dipole with $g_{10} = -190$ nT is not considered further since it is the most obviously wrong of the five models. The average standard deviations of the residuals, $\langle\sigma\text{-}\delta\rangle$, in B_ρ, B_Z, and B_T, are all in the range 4 to 11 nT. The offset dipole model yields $\langle$rms$\rangle$ values that are comparable to, or slightly larger than, the standard deviation in the residuals, indicating that any systematic signal exclusive of the offset dipole and external model is comparable to the $\langle\sigma\text{-}\delta\rangle$ values.

[40] The average residuals versus Z_{MSO} follow the same pattern as the examples. The centered dipole with $g_{10} = -300$ nT gives $B_\rho = 50$ to 100 nT more negative (positive residual) from $Z_{MSO} = 0.2$ to 0.8 R_M, whereas B_Z is too large and positive (negative residual) near the equator, $Z_{MSO} <$

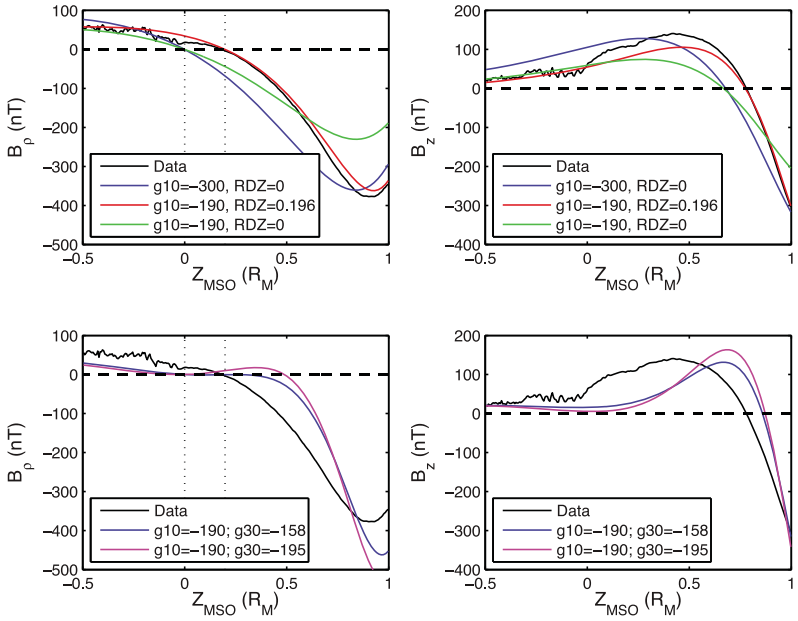

Figure 13. Comparison of observed magnetic field with different models for Mercury's internal field for 26 March 2011 (DOY 85) from 14:00:37 UTC (Z_{MSO} = 1.0 R_M) to 14:23:45 UTC (Z_{MSO} = −0.5 R_M). (left) Results for B_ρ, and (right) results for B_Z. The observations are shown in black. (top) Results for three different dipole models: an offset dipole (red); a centered dipole that matches the high-latitude field (blue); and a centered dipole with the same moment as the offset dipole (green). RDZ is the dipole offset in R_M. (bottom) Two centered dipole–octupole models, both with g_{10} = −190 nT: g_{30} = −158 nT consistent with the observed off-equator B_ρ = 0 points (blue), and g_3^0 = −195 nT (pink) to illustrate the effects of an even stronger octupole contribution. For reference: B_ρ = 0 at 14:14:13 UTC when Z_{MSO} = +0.180 R_M (439 km) and B_Z = 65.8 nT; Z_{MSO} = 0 at 14:16:44 UTC when B_ρ = 24.1 nT and B_Z = 107.9 nT. The ascending-node MSO local time and planetary longitude were 2.7 h and −142°E.

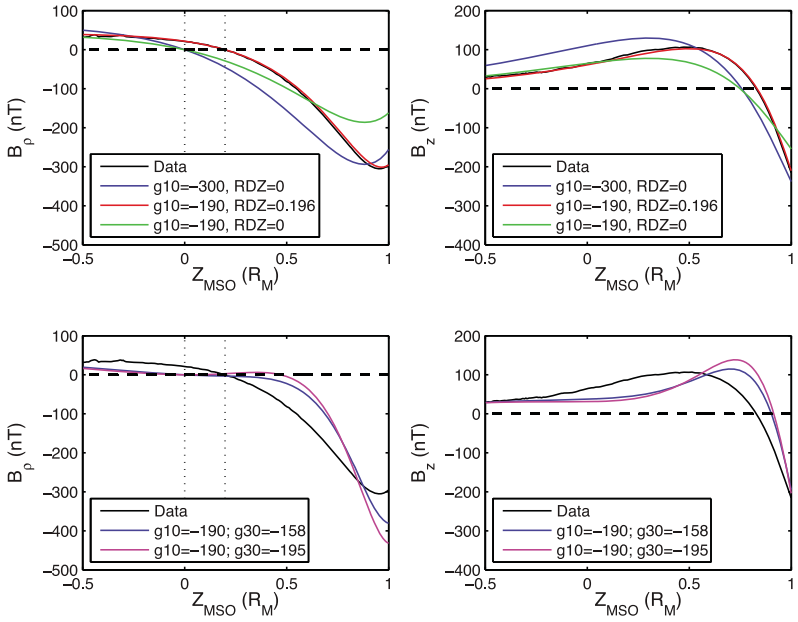

Figure 14. Comparison of observed magnetic field with different models for Mercury's internal field for 25 October 2011 (DOY 298) from 10:14:24 UTC (Z_{MSO} = 1.0 R_M) to 10:39:13 UTC (Z_{MSO} = −0.5 R_M) in the same format as Figure 13. For reference: B_ρ = 0 at 10:28:36 UTC when Z_{MSO} = +0.201 R_M (490 km) and B_Z = 86.9 nT; Z_{MSO} = 0 at 10:31:37 UTC when B_ρ = 21.1 nT and B_Z = 64.5 nT. The ascending-node MSO local time and planetary longitude were 18.3 h and −10°E.

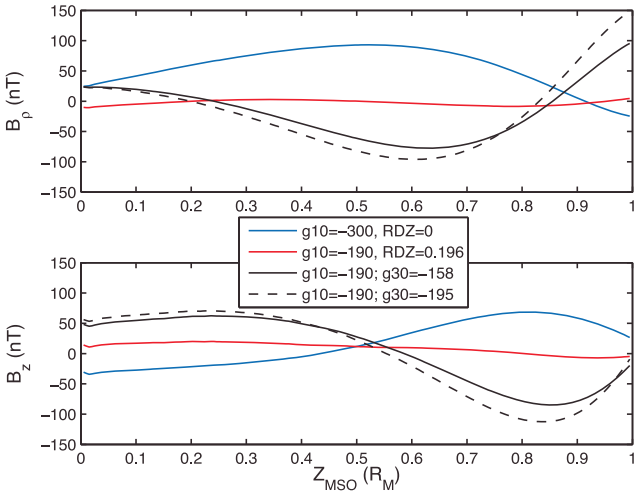

Figure 15. Average residuals of (top) B_ρ and (bottom) B_Z components of the field for the orbits listed in Table 3 as functions of Z_{MSO}. The four models considered are the offset dipole model (red); the centered dipole model with a moment that matches the high northern latitude data (blue); the dipole–octupole model that gives an off-equatorial $B_\rho = 0$ point where the near-planet crossings show the average $B_\rho = 0$ point, $g_{30} = -158$ nT (solid black); and a dipole–octupole model with a larger octupole term, $g_{30} = -195$ nT (dashed black). For the first two models, RDZ is the dipole offset in R_M. The averages over Z_{MSO} of the absolute residuals and of the standard deviations at each Z_{MSO} are given in Table 6. In every case except the offset dipole model, the standard deviations in the residuals averaged over the cases in Table 5 are much smaller than the residuals.

0.4 R_M. Both of the dipole–octupole models underestimate B_ρ for Z_{MSO} = 0.2 to 0.8 R_M by up to 70 nT, and then overestimate B_ρ near Z_{MSO} = 1 R_M by 100 to 150 nT, whereas they underestimate B_Z for $Z_{MSO} < 0.5$ R_M by ~50 nT and then overestimate B_Z near Z_{MSO} = 0.8 to 0.9 R_M by 60 to 100 nT. For these models, the ⟨rms⟩ and ⟨|δ|⟩ values are at least a factor of five greater than ⟨σ-δ⟩, indicating that the systematic residuals observed in the examples are similar for all of the events, that is, the discrepancies are similar at all longitudes.

3.2. Upper Limits to Higher-Degree Structure

[41] We use the residuals relative to the offset dipole field to assess any remaining signal that could be attributed to the axially aligned terms of degree 3 and 4 beyond that corresponding to the offset dipole (cf. Table 4). We denote these contributions by g_{30}* and g_{40}*. *Johnson et al.* [2012] found that the residuals are best organized in MSO coordinates rather than body-fixed coordinates, indicating that most of the residual signal is due to external rather than internal fields. Thus, definitive estimation of nonzero higher degree and order terms must be deferred until the external model is refined to better than the level of residuals evident in Figure 15. Here we simply fit the residuals with a two-parameter axially symmetric field model, under the assumption that the signal can be attributed to a planetary origin. The parameters are the next two highest degrees in a spherical harmonic expansion of a zonal (axially symmetric) field: g_{30}* and g_{40}*. Because we attribute all of the residual signal to internal origin, and because we estimate only two parameters, the magnitudes that we find for g_{30}* and g_{40}* will almost certainly overestimate the amplitude of these terms in the internal field. Thus, the analysis here places an empirically derived upper bound on the magnitude of the additional contribution to the axial octupole term for qualitative comparison with dynamo predictions. A similar approach has been recently used to analyze Saturn's axisymmetric field [*Cao et al.*, 2011].

[42] A grid search was performed to find the g_{30}* and g_{40}* coefficients for the best fit model to the residuals in B_r of the offset dipole model relative to the observations for the orbits in Table 5. We restricted the data to portions of the orbit where the satellite altitude was less than 600 km, to ensure maximum sensitivity to the internal field. The resulting minimum RMS misfit was 7 nT for g_{30}^*/g_{10} = 0.04 and $g_{40}^*/g_{10} = -0.07$, from which we conclude that upper limits for the coefficients are $|g_{30}^*/g_{10}|<0.04$ and $|g_{40}^*/g_{10}|<0.07$, as given in Table 4. We emphasize that the g_{40}* term in particular likely contains power aliased from higher spherical harmonic degrees and orders, and thus the results do not indicate the relative magnitude of g_{30}* and g_{40}*. The primary result for our purposes is that $|g_{30}^*/g_{20}|$ is not larger than about 0.1, so that $g_{30}/g_{20} \sim 0.29$ consistent with the offset dipole (cf. Tables 3 and 4).

4. Summary and Discussion

[43] The analyses of magnetic field equator signatures for equator crossings of the MESSENGER spacecraft on the descending node, at 1000 to 1500 km altitude, and ascending node, at 3500 to 5000 km altitude, give the same northward offset of the magnetic equator. The persistence of a northward offset in the distant altitude range confirms that the magnetic equator identification unambiguously determines

Table 6. Residual Statistics for Forward Models of Mercury's Internal Field[a]

	B_ρ			B_Z			B_T			
Model	⟨rms⟩	⟨|δ|⟩	⟨σ-δ⟩	⟨rms⟩	⟨|δ|⟩	⟨σ-δ⟩	⟨rms⟩	⟨|δ|⟩	⟨σ-δ⟩	Units
Offset dipole[b]	6	4	4	14	11	9	12	11	7	nT
$g_{10} = -300$ nT	64	60	8	42	33	11	51	48	7	nT
$g_{30} = 0.83 g_{10}$	50	40	9	56	50	12	49	47	10	nT
$g_{30} = 1.03 g_{10}$	68	53	11	69	61	13	59	53	11	nT

[a]Quantities in the table are defined as follows: δ is the residual between the observation and the model for the specified internal field model and is a function of Z_{MSO}; ⟨⟩ indicates averaging over Z_{MSO} from 0 to 1 R_M; ⟨rms⟩ is the root-mean-square misfit; ⟨|δ|⟩ is the average absolute value of δ; σ-δ is the standard deviation in δ; and ⟨σ-δ⟩ is its average over Z_{MSO}.
[b]The offset dipole model is that of *Johnson et al.* [2012]; moment = 190 nT-R_M^3, Z-axis offset = +0.196 R_M.

that the global field is best represented as a dipole offset to the north by 480 km. We note that the plasma sheet pressures are centered with respect to the magnetic equator [*Korth et al.*, 2012], providing additional confirmation of the offset. The most precise value for the offset is from the near-planet crossings, which give 479 ± 6 km, corresponding to $g_{20}/g_{10} = 0.392 \pm 0.010$. This set of crossings yields a tilt of the offset dipole axis of not more than 0.8° from the planetary rotation axis. An axially aligned dipole-octupole field cannot explain the same offset of the near and far current sheet crossings from the planetary equator. Analysis of 13 magnetically quiet orbits distributed approximately evenly in longitude reveals that the offset dipole representation with the external field of *Johnson et al.* [2012] yields residuals for these quiet orbits of ∼10 nT, or ∼2.5% of the maximum observed field in the northern polar regions. We find that g_{30} is dominated by the contribution from the offset dipole such that $g_{30}/g_{20} \sim 0.3$ and $g_{30}/g_{10} \sim 0.1$. This result is consistent with that obtained by *Uno et al.* [2009] from a regularized inversion of the Mariner 10 and MESSENGER flyby observations. Our upper limits for the higher-degree axial coefficients are also supported by inversions for high-latitude remanent crustal fields that yield g_{30}* and g_{40}* terms that are less than 1% of the axial dipole term [*Purucker et al.*, 2012].

[44] The combination of high axial alignment, large value for $|g_{20}/g_{10}|$, and low upper bound on $|g_{30}/g_{10}|$ presents a challenge to a number of dynamo models for Mercury's magnetic field. As summarized in the introduction and reviewed by *Stanley and Glatzmaier* [2010] and *Schubert and Soderlund* [2011], many candidates for producing a weak field have been proposed. Among these models, those that predict power spectra dominated by odd harmonics, such as the induction feedback dynamo [*Glassmeier et al.*, 2007a, 2007b; *Gómez-Pérez and Solomon*, 2010; *Gómez-Pérez and Wicht*, 2010; *Heyner et al.*, 2011a, 2011b] and the double iron-snow-layer model [*Vilim et al.*, 2010] are not compatible with either our large $|g_{20}/g_{10}|$ or our low $|g_{30}/g_{20}|$ ratios.

[45] One mechanism that appears to account for the observed field invokes a non-convecting layer above a deep dynamo [*Christensen*, 2006; *Christensen and Wicht*, 2008]. These models are variations on a suggestion originally proposed for Saturn [*Stevenson*, 1982]. Although the dynamo produces a field of high degree and order at the top of the convecting zone [cf. *Heimpel et al.*, 2005], the field observed exterior to the core yields only lowest degree terms because the higher-degree components of the field are sufficiently variable in time that they are highly attenuated as the field diffuses through the non-convecting, but electrically conductive, top layer of the core [*Christensen*, 2006; *Christensen and Wicht*, 2008]. In addition, differential rotation representing a thermal wind in a thick stable layer is important for preferentially attenuating the non-axisymmetric components of the low degree terms. However, the precise role of the stable layer in modifying the dynamo-produced field warrants further investigation. For example, *Stanley and Mohammadi* [2008] found that thermal winds in a thin stable layer can destabilize the field morphology and lead to surface fields that need not be large in scale and can be either strong or weak. Moreover, relaxing the computational assumption of equal diffusivity for thermal and compositional buoyancy in the stable layer yields different surface field morphologies and strengths, depending on the core sulfur content [*Manglik et al.*, 2010]. For sulfur contents of 2%, the doubly diffusive convective regime for a thermally stably stratified layer produces fingers of compositionally light fluid that penetrate the stable layer, enhancing the poloidal field and resulting in a surface field that is an order of magnitude stronger than the observed field. Sulfur contents of 0.2% lead to weaker surface fields, but these fields are quadrupole-dominated rather than dipole-dominated. Thus these studies collectively indicate that understanding the dynamics of the stable layer is critical to predicting the observed surface field.

[46] The recently determined gravity fields for Mercury [*Smith et al.*, 2012] suggest that the solid outer shell of Mercury may be too dense to be composed solely of crustal and mantle silicates compatible with surface chemical observations and may contain an iron-rich lower layer, possibly in the form of solid Fe-S at the top of the core (S. A. Hauck II et al., The curious case of Mercury's internal structure, submitted to *Journal of Geophysical Research*, 2012). A solid layer, if sufficiently electrically conductive, might also attenuate the field structure at high degree and order. Possible core compositions consistent with the gravity results are also consistent with a stably stratified top layer in the liquid core such that the dynamo occurs in the convectively unstable lower portion of the fluid core [*Smith et al.*, 2012; Hauck et al., submitted manuscript, 2012]. This inference suggests that the model of *Christensen and Wicht* [2008], which follows the proposal for the axially aligned offset dipole field for Saturn [*Stevenson*, 1982], may warrant modification to allow for a solid layer overlying a stably stratified layer in the outermost core.

[47] Measurement of the coefficients in the harmonic expansion of the internal magnetic field to higher degree and order may provide important clues to further discriminate among candidate dynamo scenarios, particularly in providing quantitative measures of higher-degree longitudinal structure. The primary challenges to resolving structure at higher degree and order are limitations on current descriptions of the external field. Even at low altitudes the external field contributes as much to the observations as the internal field, so that errors of even a few percent in the external field will contribute residuals comparable to those found here. *Johnson et al.* [2012] determined a paraboloid model for the external field tuned to match orbital constraints for the magnetopause subsolar distance, tail current sheet distance and thickness, and magnetotail lobe flux. The residuals that remain after subtracting this external field and the offset dipole internal field are well organized in MSO coordinates but are not ordered in body-fixed coordinates. This finding implies that the primary remaining signal is from the external field, and *Johnson et al.* [2012] illustrated how a change in magnetopause distance can match some of the structure in the remaining residuals. R. M. Winslow et al. (Mercury's magnetopause and bow shock from MESSENGER observations, submitted to *Journal of Geophysical Research*, 2012) examined the shape of Mercury's magnetopause and bow shock and found that the parabolic magnetopause adopted in the external field model of *Alexeev et al.* [2008, 2010] is not an accurate description of the nightside magnetopause and that the magnetosphere is nearly cylindrical rather than parabolic on the nightside [cf. *Shue et al.*, 1997].

[48] Thus, it appears that the next major advance in characterizing the internal field depends on improving the

external field description and in particular the magnetopause shape. Nonetheless, the peculiarly simple global field implies that models yielding predominantly odd harmonics in the Gauss coefficients are at variance with the observations. Whereas the model that is most consistent qualitatively with the global field is a deep dynamo with an overlying non-convecting iron-rich layer [*Christensen*, 2006; *Christensen and Wicht*, 2008], this model warrants further examination under less ideal assumptions, and continued efforts to match the observed structure with other mechanisms are needed to assess whether that structure is unique to the deep dynamo scenario.

[49] **Acknowledgments.** The MESSENGER project is supported by the NASA Discovery Program under contracts NAS5–97271 to The Johns Hopkins University Applied Physics Laboratory and NASW-00002 to the Carnegie Institution of Washington. C.L.J. and M.E.P. are supported by MESSENGER Participating Scientist grants NNX11AB84G and NNH08CC05C. R.M.W. and C.L.J. acknowledge support from the Natural Sciences and Engineering Research Council of Canada. J.E.B. is supported by the NASA CCMSM-24 Program.

References

Aharonson, O., M. T. Zuber, and C. S. Solomon (2004), Crustal remanence in an internally magnetized non-uniform shell: A possible source for Mercury's magnetic field?, *Earth Planet. Sci. Lett.*, *218*, 261–268, doi:10.1016/S0012-821X(03)00682-4.

Alexeev, I. I., E. S. Belenkaya, S. Y. Bobrovnikov, J. A. Slavin, and M. Sarantos (2008), Paraboloid model of Mercury, *J. Geophys. Res.*, *113*, A12210, doi:10.1029/2008JA013368.

Alexeev, I. I., et al. (2010), Mercury's magnetospheric magnetic field after the first two MESSENGER flybys, *Icarus*, *209*, 23–39, doi:10.1016/j.icarus.2010.01.024.

Anderson, B. J., M. H. Acuña, D. A. Lohr, J. Scheifele, A. Raval, H. Korth, and J. A. Slavin (2007), The Magnetometer instrument on MESSENGER, *Space Sci. Rev.*, *131*, 417–450, doi:10.1007/s11214-007-9246-7.

Anderson, B. J., M. H. Acuña, H. Korth, M. E. Purucker, C. L. Johnson, J. A. Slavin, S. C. Solomon, and R. L. McNutt Jr. (2008), The magnetic field of Mercury: New constraints on structure from MESSENGER, *Science*, *321*, 82–85, doi:10.1126/science.1159081.

Anderson, B. J., et al. (2010), The magnetic field of Mercury, *Space Sci. Rev.*, *152*, 307–339, doi:10.1007/s11214-009-9544-3.

Anderson, B. J., C. L. Johnson, H. Korth, M. E. Purucker, R. M. Winslow, J. A. Slavin, S. C. Solomon, R. L. McNutt Jr., J. M. Raines, and T. H. Zurbuchen (2011), The global magnetic field of Mercury from MESSENGER orbital observations, *Science*, *333*, 1859–1862, doi:10.1126/science.1211001.

Bartels, J. (1936), The eccentric dipole approximating the Earth's magnetic field, *J. Geophys. Res.*, *41*, 225–250, doi:10.1029/TE041i003p00225.

Borovsky, J. E. (2012), Looking for evidence of mixing in the solar wind from 0.31 to 0.98 AU, *J. Geophys. Res.*, *117*, A06107, doi:10.1029/2012JA017525.

Cao, H., C. T. Russell, U. R. Christensen, M. K. Dougherty, and M. E. Burton (2011), Saturn's very axisymmetric magnetic field: No detectable secular variation or tilt, *Earth Planet. Sci. Lett.*, *304*, 22–28, doi:10.1016/j.epsl.2011.02.035.

Christensen, U. R. (2006), A deep dynamo generating Mercury's magnetic field, *Nature*, *444*, 1056–1058, doi:10.1038/nature05342.

Christensen, U. R., and J. Wicht (2008), Models of magnetic field generation in partly stable planetary cores: Applications to Mercury and Saturn, *Icarus*, *196*, 16–34, doi:10.1016/j.icarus.2008.02.013.

Giampieri, G., and A. Balogh (2002), Mercury's thermoelectric dynamo revisited, *Planet. Space Sci. 50*, 757–762.

Glassmeier, K.-H., H.-U. Auster, and U. Motschmann (2007a), A feedback dynamo generating Mercury's magnetic field, *Geophys. Res. Lett.*, *34*, L22201, doi:10.1029/2007GL031662.

Glassmeier, K.-H., J. Grosser, U. Auster, D. Constantinescu, Y. Narita, and S. Stellmach (2007b), Electromagnetic induction effects and dynamo action in the Hermean system, *Space Sci. Rev.*, *132*, 511–527, doi:10.1007/s11214-007-9244-9.

Gómez-Pérez, N., and S. C. Solomon (2010), Mercury's weak magnetic field: A result of magnetospheric feedback?, *Geophys. Res. Lett.*, *37*, L20204, doi:10.1029/2010GL044533.

Gómez-Pérez, N., and J. Wicht (2010), Behavior of planetary dynamos under the influence of external magnetic fields: Application to Mercury and Ganymede, *Icarus*, *209*, 53–62, doi:10.1016/j.icarus.2010.04.006.

Heimpel, M., J. M. Aurnou, F. M. Al-Shamali, and N. Gomez Perez (2005), A numerical study of dynamo action as a function of spherical shell geometry, *Earth Planet. Sci. Lett.*, *236*, 542–557, doi:10.1016/j.epsl.2005.04.032.

Heyner, D., D. Schmitt, K.-H. Glassmeier, and J. Wicht (2011a), Dynamo action in an ambient field, *Astron. Nachr.*, *332*, 36–42, doi:10.1002/asna.201011466.

Heyner, D., J. Wicht, N. Gómez-Pérez, D. Schmitt, H.-U. Auster, and K.-H. Glassmeier (2011b), Evidence from numerical experiments for a feedback dynamo generating Mercury's magnetic field, *Science*, *334*, 1690–1693, doi:10.1126/science.1207290.

Johnson, C. L., et al. (2012), MESSENGER observations of Mercury's magnetic field structure, *J. Geophys. Res.*, doi:10.1029/2012JE004217, in press.

Korth, H., B. J. Anderson, M. H. Acuña, J. A. Slavin, N. A. Tsyganenko, S. C. Solomon, and R. L. McNutt Jr. (2004), Determination of the properties of Mercury's magnetic field by the MESSENGER mission, *Planet. Space Sci.*, *52*, 733–746, doi:10.1016/j.pss.2003.12.008.

Korth, H., B. J. Anderson, J. M. Raines, J. A. Slavin, T. H. Zurbuchen, C. L. Johnson, M. E. Purucker, R. M. Winslow, S. C. Solomon, and R. L. McNutt Jr. (2011), Plasma pressure in Mercury's equatorial magnetosphere derived from MESSENGER Magnetometer observations, *Geophys. Res. Lett.*, *38*, L22201, doi:10.1029/2011GL049451.

Korth, H., B. J. Anderson, C. L. Johnson, R. M. Winslow, J. A. Slavin, M. E. Purucker, S. C. Solomon, and R. L. McNutt Jr. (2012), Characteristics of the plasma distribution in Mercury's equatorial magnetosphere derived from MESSENGER Magnetometer observations, *J. Geophys. Res.*, doi:10.1029/2012JA018052, in press.

Manglik, A., J. Wicht, and U. R. Christensen (2010), A dynamo model with double diffusive convection for Mercury's core, *Earth Planet. Sci. Lett.*, *289*, 619–628, doi:10.1016/j.epsl.2009.12.007.

Margot, J. L., S. J. Peale, R. F. Jurgens, M. A. Slade, and I. V. Holin (2007), Large longitude libration of Mercury reveals a molten core, *Science*, *316*, 710–714, doi:10.1126/science.1140514.

Ness, N. F., K. W. Behannon, R. P. Lepping, Y. C. Whang, and K. H. Schatten (1974), Magnetic field observations near Mercury: Preliminary results, *Science*, *185*, 151–160, doi:10.1126/science.185.4146.151.

Ness, N. F., K. W. Behannon, R. P. Lepping, and Y. C. Whang (1975), The magnetic field of Mercury, 1, *J. Geophys. Res.*, *80*, 2708–2716, doi:10.1029/JA080i019p02708.

Olson, P., and U. R. Christensen (2006), Dipole moment scaling for convection-driven planetary dynamos, *Earth Planet. Sci. Lett.*, *250*, 561–571, doi:101.1016/j.epsl.2006.08.008.

Purucker, M. M., T. J. Sabaka, S. C. Solomon, B. J. Anderson, H. Korth, M. T. Zuber, and G. A. Neumann, (2009), Mercury's internal magnetic field: Constraints on large- and small-scale fields of crustal origin, *Earth Planet. Sci. Lett.*, *285*, 340–346, doi:10.1016/j.epsl.2008.12.017.

Purucker, M. E., et al. (2012), Evidence for a crustal magnetic signature on Mercury from MESSENGER observations, *Lunar Planet. Sci.*, *43*, Abstract 1297.

Rosenbauer, H., R. Schwenn, E. Marsch, B. Meyer, H. Miggenrieder, M. D. Montgomery, K. H. Muhlhauser, W. Pilipp, W. Voges, and S. M. Zink (1977), A survey on initial results of the Helios plasma experiment, *J. Geophys.*, *42*, 561–580.

Schubert, G., and K. M. Soderlund (2011), Planetary magnetic fields: Observations and models, *Phys. Earth Planet. Inter.*, *187*, 92–108, doi:10.1016/j.pepi.2011.05.013.

Shue, J.-H., J. K. Chao, H. C. Fu, C. T. Russell, P. Song, K. K. Khurana, and H. J. Singer (1997), A new functional form to study the solar wind control of the magnetopause size and shape, *J. Geophys. Res.*, *102*, 9497–9511, doi:10.1029/97JA00196.

Slavin, J. A., et al. (2010), MESSENGER observations of extreme loading and unloading of Mercury's magnetic tail, *Science*, *329*, 665–668, doi:10.1126/science.1188067.

Slavin, J. A., et al. (2012), MESSENGER observations of a flux-transfer-event shower at Mercury, *J. Geophys. Res.*, *117*, A00M06, doi:10.1029/2012JA017926.

Smith, D. E., et al. (2012), Gravity field and internal structure of Mercury from MESSENGER, *Science*, *336*, 214–217, doi:10.1126/science.1218809.

Solomon, S. C., R. L. McNutt Jr., R. E. Gold, and D. L. Domingue (2007), MESSENGER mission overview, *Space Sci. Rev.*, *131*, 3–39, doi:10.1007/s11214-007-9247-6.

Stanley, S., and G. A. Glatzmaier (2010), Dynamo models for planets other than Earth, *Space Sci. Rev.*, *152*, 617–649, doi:10.1007/s11214-009-9573-y.

Stanley, S., and A. Mohammadi (2008), Effects of an outer thin stably stratified layer on planetary dynamos, *Phys. Earth Planet. Inter.*, *168*, 179–190, doi:10.1016/j.pepi.2008.06.016.

Stanley, S., J. Bloxham, W. E. Hutchison, and M. T. Zuber (2005), Thin shell dynamo models consistent with Mercury's weak observed magnetic field, *Earth Planet. Sci. Lett.*, *234*, 27–38, doi:10.1016/j.epsl.2005.02.040.

Stevenson, D. J. (1982), Reducing the non-axisymmetry of a planetary dynamo and an application to Saturn, *Geophys. Astrophys. Fluid Dyn.*, *21*, 113–127, doi:10.1080/03091928208209008.

Stevenson, D. J. (1987), Mercury's magnetic field–A thermoelectric dynamo?, *Earth Planet. Sci. Lett.*, *82*, 114–120, doi:10.1016/0012-821X(87)90111-7.

Stevenson, D. J. (2003), Planetary magnetic fields, *Earth Planet. Sci. Lett.*, *208*, 1–11, doi:10.1016/S0012-821X(02)01126-3.

Sundberg, T., et al. (2012), MESSENGER observations of dipolarization events in Mercury's magnetotail, *J. Geophys. Res.*, *117*, A00M03, doi:10.1029/2012JA017756.

Takahashi, F., and M. Matsushima (2006), Dipolar and non-dipolar dynamos in thin spherical shell geometry with implications for the magnetic field of Mercury, *Geophys. Res. Lett.*, *33*, L10202, doi:10.1029/2006GL025792.

Uno, H., C. L. Johnson, B. J. Anderson, H. Korth, and S. C. Solomon (2009), Mercury's internal magnetic field: Constraints from regularized inversions, *Earth Planet. Sci. Lett.*, *285*, 328–339, doi:10.1016/j.epsl.2009.02.032.

Vilim, R., S. Stanley, and S. A. Hauck II (2010), Iron snow zones as a mechanism for generating Mercury's weak observed magnetic field, *J. Geophys. Res.*, *115*, E11003, doi:10.1029/2009JE003528.

Wicht, J., M. Mandea, F. Takahashi, U. R. Christensen, M. Matushima, and B. Langlais (2007), The origin of Mercury's internal magnetic field, *Space Sci. Rev.*, *132*, 261–290, doi:10.1007/s11214-007-9280-5.

Winslow, R. M., C. L. Johnson, B. J. Anderson, H. Korth, J. A. Slavin, M. E. Purucker, and S. C. Solomon (2012), Observations of Mercury's northern cusp region with MESSENGER's Magnetometer, *Geophys. Res. Lett.*, *39*, L08112, doi:10.1029/2012GL051472.

Zurbuchen, T. H., et al. (2011), MESSENGER observations of the spatial distribution of planetary ions near Mercury, *Science*, *333*, 1862–1865, doi:10.1126/science.1211302.